



**HAL**  
open science

## Learning acoustic responses from experiments: A multiscale-informed transfer learning approach

van Hai Trinh, Johann Guilleminot, Camille Perrot, Viet Dung Vu

► **To cite this version:**

van Hai Trinh, Johann Guilleminot, Camille Perrot, Viet Dung Vu. Learning acoustic responses from experiments: A multiscale-informed transfer learning approach. *Journal of the Acoustical Society of America*, 2022, 151 (4), pp.2587-2601. 10.1121/10.0010187 . hal-03683777

**HAL Id: hal-03683777**

**<https://hal.science/hal-03683777>**

Submitted on 31 May 2022

**HAL** is a multi-disciplinary open access archive for the deposit and dissemination of scientific research documents, whether they are published or not. The documents may come from teaching and research institutions in France or abroad, or from public or private research centers.

L'archive ouverte pluridisciplinaire **HAL**, est destinée au dépôt et à la diffusion de documents scientifiques de niveau recherche, publiés ou non, émanant des établissements d'enseignement et de recherche français ou étrangers, des laboratoires publics ou privés.

**Learning acoustic responses from experiments: A multiscale-informed transfer learning approach**

Van Hai Trinh,<sup>1</sup> Johann Guilleminot,<sup>2, a</sup> Camille Perrot,<sup>3, b</sup> and Viet Dung Vu<sup>4</sup>

<sup>1</sup>*Faculty of Vehicle and Energy Engineering, Le Quy Don Technical University, 236, Hoang Quoc Viet, Ha Noi, Vietnam*

<sup>2</sup>*Department of Civil and Environmental Engineering, Duke University, Durham, NC 27708, USA*

<sup>3</sup>*Univ Gustave Eiffel, Univ Paris Est Creteil, CNRS, UMR 8208, MSME, F-77454 Marne-La-Vallée, France*

<sup>4</sup>*Department of Mechanical Engineering, Université de Sherbrooke, Sherbrooke, Quebec J1K 2R1, Canada*

(Dated: 31 May 2022)

1 A methodology to learn acoustical responses based on limited experimental datasets  
2 is presented. From a methodological standpoint, the approach involves a multiscale-  
3 informed encoder, used to cast the learning task in a finite-dimensional setting. A  
4 neural network model mapping parameters of interest to the latent variables is then  
5 constructed and calibrated using transfer learning and knowledge gained from the  
6 multiscale surrogate. The relevance of the approach is assessed by considering the  
7 prediction of the sound absorption coefficient for randomly-packed rigid spherical  
8 beads of equal diameter. A two-microphone method is used, in this context, to mea-  
9 sure the absorption coefficient on a set of configurations with various monodisperse  
10 particle diameters and sample thicknesses, and a hybrid numerical approach relying  
11 on the Johnson-Champoux-Allard-Pride-Lafarge (JCAPL) model is deployed as the  
12 multiscale-based predictor. It is shown that the strategy allows for the relationship  
13 between the micro-/structural parameters and the experimental acoustic response to  
14 be well approximated, even if a small physical dataset (comprised of ten samples) is  
15 used for training. The methodology therefore enables the identification and valida-  
16 tion of acoustical models under constraints related to data limitation and parametric  
17 dependence. It also paves the way for an efficient exploration of the parameter space  
18 for acoustical materials design.

---

<sup>a</sup>[johann.guillemot@duke.edu](mailto:johann.guillemot@duke.edu)

<sup>b</sup>[camille.perrot@univ-eiffel.fr](mailto:camille.perrot@univ-eiffel.fr)

19 **I. INTRODUCTION**

20 The analysis of the relationship between microstructural parameters and ultimate acous-  
21 tic performance is a fundamental question that has attracted much attention over the past  
22 two decades. Various frameworks and variations thereof were proposed to understand the  
23 underlying physical mechanisms and to predict acoustical properties for different types  
24 of materials, including the use of purely phenomenological,<sup>1-4</sup> semi-phenomenological,<sup>5-10</sup>  
25 semi-analytical,<sup>11-13</sup> and multiscale models;<sup>14-17</sup> see Refs.<sup>18,19</sup> for a review. Most of these  
26 approaches are found to produce reasonably accurate estimations within their respective  
27 range of applicability, even if some discrepancies between model predictions and exper-  
28 imental responses are sometimes observed for certain classes of materials, such as non-  
29 linear metamaterials.<sup>20,21</sup> While a large body of the literature has focused on bottom-up  
30 approaches, predicting acoustic performance based on microstructural descriptors, the re-  
31 lationship may also be investigated as a top-down approach, solving an inverse problem  
32 to infer microstructural parameters based on coarse-scale measurements. In this context,  
33 the Bayesian approach to parameter identification was applied in Ref.<sup>22</sup> to calibrate the  
34 geometrical, transport, and elastic properties characterizing the elasto-acoustic behavior of  
35 poro-elastic materials. More recently, so-called data-driven approaches have emerged with  
36 the aim of learning forward or inverse models based on datasets. The use of neural network  
37 models, in particular, was proposed as a means to represent potentially highly nonlinear  
38 maps in very high-dimensional settings (see Ref.<sup>23</sup> for a review in acoustics, as well as Ref.<sup>24</sup>  
39 for an application involving convolutional neural networks). Physics-informed formulations

40 involving residuals from parametric partial differential equations were proposed to bridge the  
41 gap between established physical theories and approaches solely relying on data science (see  
42 the seminal work,<sup>25</sup> for instance). Deep learning techniques are often meant to be operated  
43 in the big data limit, that is, for very large datasets. This assumption may be deemed inad-  
44 equate in scientific machine learning where practical applications typically involve limited  
45 physical experiments.

46 The goal of this work is to propose a methodology that circumvents data limitation  
47 for learning experimental acoustic responses parameterized by microstructural and sam-  
48 ple properties. Specifically, we address the calibration of a neural network model using a  
49 small dataset—typically comprised of a few experimental results—by leveraging informa-  
50 tion gained through a standard multiscale analysis. It is important to emphasize at this  
51 point that the aim of this study is not to assess the performance or to promote the use of  
52 one class of methods against the other (that is, physics-based versus data-driven models),  
53 for a specific regression problem. We rather focus on the development of a methodology  
54 that combines these two ingredients in a synergistic manner, to address a question that  
55 remains hard to tackle using any of these methods independently. Borrowing ingredients  
56 from multi-fidelity modeling<sup>26</sup> and operator learning<sup>27</sup>, we first introduce an appropriate  
57 simulation-based representation that encodes the experimental response in the frequency  
58 domain. Here, we consider the prediction of the sound absorption coefficient as a proto-  
59 typical application. We then develop a neural network model between input parameters of  
60 interest and the reduced variables defined by the encoder. We finally use a transfer learning  
61 approach to compensate for data scarcity at the training stage.

62 This paper is organized as follows. The overall methodology and technical ingredients are  
 63 presented in Sec. II. We discuss, in particular, the encoding-decoding strategy and learning  
 64 aspects. We then deploy and analyze the performance of the approach in Sec. III. We  
 65 specifically consider the case of sound absorption measurements and introduce both the  
 66 experimental setting and the associated computational surrogate model. We show that  
 67 the framework enables the prediction of experimental results with a fairly good accuracy  
 68 (quantified in the  $L^2$  sense), even with limited data. Concluding remarks are finally provided  
 69 in Sec. IV.

## 70 II. METHODOLOGY

### 71 A. Overview of the approach

72 We seek a surrogate model mapping some input (material or microstructural) parameters  
 73 to the sound absorption coefficient over some angular frequency range, denoted by  $\mathbb{W}$ . Let  
 74  $\boldsymbol{\mu} \mapsto \{\alpha(\omega; \boldsymbol{\mu}), \omega \in \mathbb{W}\}$  be the forward map of interest, where  $\boldsymbol{\mu}$  is the vector of input  
 75 parameters,  $\alpha$  is the sound absorption coefficient, and  $\mathbb{W}$  is assumed to be the Cartesian  
 76 product of closed intervals. Our goal is to construct a methodology that allows one to learn  
 77 this forward map, using results from a *limited* set of physical experiments.

78 Owing to a probabilistic interpretation of  $\boldsymbol{\mu}$ , which is assumed to be defined on some  
 79 probability space  $(\Theta, \mathcal{F}, P)$  (where  $\Theta$  denotes the sample space,  $\mathcal{F}$  is a  $\sigma$ -field, and  $P$  is a  
 80 probability measure), and assuming that  $\alpha \in L^2(\Theta, L^2(\mathbb{W}))$  (notice that  $\alpha$  is of second-order  
 81 as it is bounded almost surely), the process  $\{\alpha(\omega), \omega \in \mathbb{W}\}$  can be represented through its

82 Karhunen-Loève (KL) expansion<sup>28</sup>:

$$\alpha(\omega) = \underline{\alpha}(\omega) + \sum_{i=1}^{+\infty} \sqrt{\lambda_i} \eta_i \varphi_i(\omega), \quad (1)$$

83 where  $\omega \mapsto \underline{\alpha}(\omega)$  is the mean function of the sound absorption coefficient (that is,  $\underline{\alpha}(\omega) =$   
 84  $\mathbb{E}\{\alpha(\omega)\}$  for all  $\omega \in \mathbb{W}$ ), the pairs  $\{(\lambda_i, \varphi_i)\}_{i \geq 1}$  are the eigenvalues and eigenfunctions of the  
 85 covariance operator satisfying the integral equation

$$\int_{\mathbb{W}} C(\omega, \omega') \varphi_i(\omega') d\omega' = \lambda_i \varphi_i(\omega), \quad (2)$$

86 where  $(\omega, \omega') \mapsto C(\omega, \omega')$  is the covariance function of  $\{\alpha(\omega), \omega \in \mathbb{W}\}$ , and the reduced  
 87 variables  $\{\eta_i\}_{i \geq 1}$  are defined as

$$\eta_i = \frac{1}{\sqrt{\lambda_i}} \langle \alpha - \underline{\alpha}, \varphi_i \rangle, \quad (3)$$

88 with  $\langle \cdot, \cdot \rangle$  the inner product between functions:

$$\langle f, g \rangle = \int_{\mathbb{W}} f(\omega) g(\omega) d\omega. \quad (4)$$

89 The variables  $\{\eta_i\}_{i \geq 1}$  are centered, have unit variance, and are pairwise uncorrelated. Notice  
 90 that we did not adapt the notation to reflect the stochastic interpretation in the above  
 91 equations, for simplicity. The truncated expansion reads as

$$\alpha_\nu(\omega) = \underline{\alpha}(\omega) + \sum_{i=1}^{\nu} \sqrt{\lambda_i} \eta_i \varphi_i(\omega), \quad (5)$$

92 where the order  $\nu$  is determined through a convergence analysis and  $\alpha_\nu$  converges to  $\alpha$  in  
 93 the mean-square sense as  $\nu \rightarrow +\infty$ .

94 One natural path to learn the mapping  $\boldsymbol{\mu} \mapsto \{\alpha(\omega); \boldsymbol{\mu}\}, \omega \in \mathbb{W}\}$  then consists (i) in  
 95 estimating the mean  $\underline{\alpha}$  and the set of eigenpairs  $\{(\lambda_i, \varphi_i)\}_i^\nu$  from a given dataset, and (ii)

96 in learning the mapping  $\boldsymbol{\mu} \mapsto \boldsymbol{\eta}(\boldsymbol{\mu})$  between the input parameters and the latent reduced  
 97 variables, with  $\boldsymbol{\eta}(\boldsymbol{\mu}) = (\eta_1(\boldsymbol{\mu}), \dots, \eta_\nu(\boldsymbol{\mu}))^T$ . There are two main benefits of proceeding this  
 98 way. First, the learning task is now cast in a finite dimensional space (that is, in  $\mathbb{R}^\nu$ ), as  
 99 proposed in Ref.<sup>27</sup>, e.g., for the learning between Hilbert spaces for instance. Second, the  
 100 use of a basis in the frequency domain renders the approximation more robust to noise in  
 101 the data. Since we are interested in learning from experiments, it is convenient to introduce  
 102 the following truncated decomposition, related to observations:

$$\alpha_\nu^{\text{exp}}(\omega) = \underline{\alpha}^{\text{exp}}(\omega) + \sum_{i=1}^{\nu} \sqrt{\lambda_i^{\text{exp}}} \eta_i^{\text{exp}} \varphi_i^{\text{exp}}(\omega). \quad (6)$$

103 In Eq. (6), the superscript “exp” indicates that all quantities are computed based on the  
 104 experimental results, using statistical estimators. In a standard setting where few samples  
 105 are available (meaning that the physical experiments are conducted for a few choices of  
 106 input parameters, typically less than 10), the covariance operator estimated from the data  
 107 is, however, often found to be non-positive, hence making the above formulation ill-posed.  
 108 To circumvent that limitation and properly set up the learning task, we propose the following  
 109 two-step “regularization” approach.

110 (i) First, a numerical multiscale-informed surrogate model for the experiments is intro-  
 111 duced. We denote by  $\{\alpha^{\text{sim}}(\omega), \omega \in \mathbb{W}\}$  the sound absorption coefficient thus obtained,  
 112 and we consider the truncated KL expansion

$$\alpha_\nu^{\text{sim}}(\omega) = \underline{\alpha}^{\text{sim}}(\omega) + \sum_{i=1}^{\nu} \sqrt{\lambda_i^{\text{sim}}} \eta_i^{\text{sim}} \varphi_i^{\text{sim}}(\omega), \quad (7)$$

113 with notation analogous to Eq. (6).



114 (ii) Second, the (centered) experimental data are projected onto the computational basis:

115

$$\alpha_\nu^{\text{exp}}(\omega) = \underline{\alpha}^{\text{exp}}(\omega) + \sum_{i=1}^{\nu} \sqrt{\lambda_i^{\text{sim}}} \hat{\eta}_i^{\text{exp}} \varphi_i^{\text{sim}}(\omega), \quad (8)$$

116 where the same truncation order is assumed, without loss of generality, and

$$\hat{\eta}_i^{\text{exp}} := \frac{1}{\sqrt{\lambda_i^{\text{sim}}}} \langle \alpha^{\text{exp}} - \underline{\alpha}^{\text{exp}}, \varphi_i^{\text{sim}} \rangle. \quad (9)$$

117 The hat symbol in Eq. (9) is used to emphasize that the reduced coordinates are

118 different from those in Eq. (6) (see the remark below). The mapping  $\boldsymbol{\mu} \mapsto \hat{\boldsymbol{\eta}}^{\text{exp}}(\boldsymbol{\mu})$

119 is subsequently approximated by using transfer learning with neural network models,

120 using prior knowledge gained by developing a surrogate model for the mapping  $\boldsymbol{\mu} \mapsto$

121  $\boldsymbol{\eta}^{\text{sim}}(\boldsymbol{\mu})$ .

122 It should be noticed that the above approach can be interpreted, to some extent, in a

123 multi-fidelity setting where  $\alpha^{\text{exp}}$  represents information that is costly to collect, while the

124 numerical approximation  $\alpha^{\text{sim}}$  remains cheaper to synthesize in general. A study about

125 transfer learning in this context can be found in Ref.<sup>26</sup> for instance. Moreover, the use

126 of a KL expansion rises theoretical issues pertaining to approximation capabilities for the

127 neural networks, due to the non-compactness of the latent spaces. This fundamental aspect

128 is beyond the scope of this work, and we refer to Ref.<sup>27</sup> for a discussion. The ingredients of

129 the above framework are presented in the following sections.

130 *Remark:* It is important to note that Eq. (8) does not correspond to the KL expansion

131 of the process  $\{\alpha^{\text{exp}}(\omega), \omega \in \mathbb{W}\}$ . In particular, the right-hand side is not optimal in the  $L^2$

132 sense and the reduced variables  $\{\hat{\eta}_i\}_{i=1}^{\nu}$ , while centered, are not pairwise uncorrelated. The

133 representation is, however, licit since  $\{\varphi_i^{\text{sim}}\}_{i \geq 1}$  constitutes an orthonormal basis of  $L^2(\mathbb{W})$   
 134 (which follows from the properties of the covariance operator).

## 135 **B. Neural networks as surrogate models**

136 In this section, we recall the necessary background on (feed-forward) neural networks and  
 137 transfer learning. Providing general reviews on these very active research topics is beyond  
 138 the scope of this work, and we refer interested readers to Ref.<sup>29</sup> and Refs.<sup>30,31</sup> for discussions,  
 139 for instance.

### 140 **1. Background**

141 A neural network surrogate aims to map some input vector-valued parameter  $\mathbf{x} \in \mathbb{R}^{\mathcal{I}}$  to  
 142 some output (vector-valued) parameter  $\mathbf{y} \in \mathbb{R}^{\mathcal{O}}$ , using a composite transformation that (i)  
 143 involves input and output layers, as well as so-called hidden layers that each contains a set  
 144 of neurons; (ii) is learned on a training data set  $\mathcal{D} = \{\mathbf{x}^{(i)}, \mathbf{y}^{(i)}\}_{i=1}^{N_D}$  with  $N_D$  data points.  
 145 Following standard notation, we denote by  $N_H$  the total number of hidden layers, and let  $n_\ell$   
 146 be the number of neurons in the  $\ell$ th layer. In this work, we consider a feed-forward neural  
 147 network in which the output of the  $j$ th neuron in a given layer is produced by transmitting  
 148 a weighted sum of input signals (from the preceding layer), plus a bias, to an activation (or  
 149 transfer) function  $\phi_a$ :

$$z_j^{(\ell)} = \phi_a \left( \sum_{i=1}^{n_{\ell-1}} W_{ij}^{(\ell)} z_i^{(\ell-1)} + \theta_j^{(\ell)} \right), \quad 1 \leq j \leq n_\ell, \quad 1 \leq \ell \leq N_H, \quad (10)$$

150 with  $z_i^{(0)} = x_i$ ,  $1 \leq i \leq \mathcal{I}$ . The components of the output layer are defined as

$$y_j = \sum_{i=1}^{n_{N_H}} W_{ij}^{(0)} z_i^{(N_H)} + \theta_j^{(0)}, \quad 1 \leq j \leq \mathcal{O}. \quad (11)$$

151 In the above equations,  $W_{ij}^{(\ell)}$  denotes the weight for the connection between the  $i$ th neuron  
 152 in layer  $(\ell - 1)$  and the  $j$ th neuron in layer  $\ell$ , and  $\theta_j^{(\ell)}$  is the bias corresponding to the  $j$ th  
 153 neuron in layer  $\ell$ . The neural network is therefore parameterized by the sets  $\{\mathbf{W}^{(\ell)}\}_{\ell=0}^{N_H}$  and  
 154  $\{\boldsymbol{\theta}^{(\ell)}\}_{\ell=0}^{N_H}$  of weight matrices and bias vectors, where  $\mathbf{W}^{(0)}$  and  $\boldsymbol{\theta}^{(0)}$  are associated with the  
 155 output layer by convention, and

$$\mathbf{W}^{(\ell)} = [W_{ij}^{(\ell)}] \in \mathbb{M}_{n^{(\ell-1)} \times n^{(\ell)}}(\mathbb{R}), \quad \boldsymbol{\theta}^{(\ell)} = [\theta_j^{(\ell)}] \in \mathbb{M}_{1 \times n^{(\ell)}}(\mathbb{R}). \quad (12)$$

156 There exist many choices for the activation function, including the Rectified Linear Unit  
 157 (ReLU), sigmoid, and hyperbolic tangent functions for instance; see Ref.<sup>29</sup>. In this paper,  
 158 we use the sigmoid function  $\phi_a(v) = 1/[1+\exp(-v)]$  for all hidden layers, and the architecture  
 159 of the neural networks was determined through parametric analyses on validation errors.

160 An important step while using neural networks pertains to training, that is, to the calibra-  
 161 tion of the weight matrices  $\{\mathbf{W}^{(\ell)}\}_{\ell=0}^{N_H}$  and bias vectors  $\{\boldsymbol{\theta}^{(\ell)}\}_{\ell=0}^{N_H}$ . This is commonly achieved  
 162 by minimizing a loss function, potentially supplemented with a regularization term, and  
 163 many techniques were proposed in the literature.<sup>29</sup> We use a standard supervised approach  
 164 based on the minimization of the mean squared error

$$\mathcal{L}(\{\mathbf{W}^{(\ell)}, \boldsymbol{\theta}^{(\ell)}\}_{\ell=0}^{N_H}) = \frac{1}{N_D} \sum_{i=1}^{N_D} \|\hat{\mathbf{y}}(\mathbf{x}^{(i)}; \{\mathbf{W}^{(\ell)}, \boldsymbol{\theta}^{(\ell)}\}_{\ell=0}^{N_H}) - \mathbf{y}^{(i)}\|^2, \quad (13)$$

165 where  $\hat{\mathbf{y}}(\mathbf{x}^{(i)}; \{\mathbf{W}^{(\ell)}, \boldsymbol{\theta}^{(\ell)}\}_{\ell=0}^{N_H})$  denotes the prediction of the neural network parameterized by  
 166  $\{\mathbf{W}^{(\ell)}, \boldsymbol{\theta}^{(\ell)}\}_{\ell=0}^{N_H}$  at the data point  $\mathbf{x}^{(i)}$ .

167 In this work, various algorithms for network training were tested through parametric  
 168 analyses, including the Levenberg-Marquardt and stochastic gradient descent techniques.  
 169 Most algorithms were found to provide similar results, and the results provided in Sec. III C  
 170 were obtained with the Levenberg-Marquardt optimizer.

## 171 2. *Transfer learning*

172 In the context of inductive learning for regression problems (see Refs.<sup>30,31</sup> for reviews  
 173 with applications to classification and regression), transfer learning proceeds by adapting an  
 174 existing neural network that has been pretrained on data generated by a similar problem.  
 175 This principle is schematically depicted in Fig. 1, using the terminology introduced in the  
 176 aforementioned references.

178 The adaptation can be performed, for instance, by preserving the structure of the pre-  
 179 trained network and by updating its parameters in either all or a few layers, or by adding  
 180 hidden layers to approximate the mapping  $\boldsymbol{\eta}^{\text{sim}} \mapsto \hat{\boldsymbol{\eta}}^{\text{exp}}(\boldsymbol{\eta}^{\text{sim}})$ . In this work, we use the  
 181 second approach given the analogy between Eq. (7) and Eq. (8), where  $\alpha^{\text{sim}}$  is assumed to  
 182 be a reasonable proxy for  $\alpha^{\text{exp}}$ .

## 183 III. APPLICATION TO EXPERIMENTAL MEASUREMENTS FOR THE SOUND 184 ABSORPTION COEFFICIENT

185 In this section, we deploy the methodology presented in Sec. II A. The experimental  
 186 analysis is first presented in Sec. III A. The multiscale surrogate used for computing the

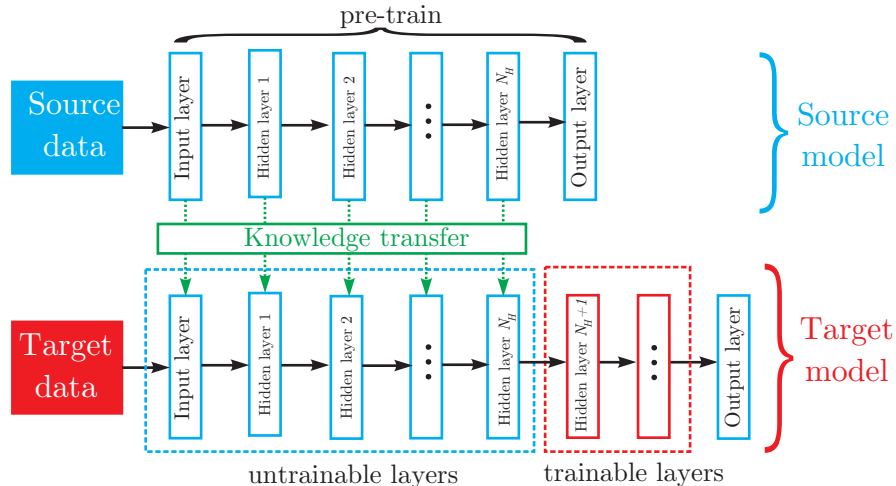


FIG. 1. Principles of transfer learning for regression problems. A neural network is first pretrained using data from a similar problem, associated with a source model (top row). Knowledge gained through this training is subsequently transferred to train an adapted neural network surrogate for the target model (bottom row). Here, this adaptation corresponds to an extension of the pretrained model through the addition of hidden layers.

187 projection basis and transfer learning is then discussed in Sec. III B. The learning strategy  
 188 is finally exemplified in Sec. III C.

189 Owing to a slight abuse of notation, we consider the sound absorption coefficient to be  
 190 expressed as a function of the angular frequency  $\omega$  or the frequency  $f$  (with  $\omega = 2\pi f$ ), and  
 191 denote by  $\alpha$  the aforementioned coefficient regardless of the associated variable.

## 192 A. Description of the physical experiments

193 In order to illustrate the approach, we consider the characterization of the sound ab-  
 194 sorption coefficient for randomly-packed rigid spherical beads. To that end, ten samples

195 with various combinations of monodisperse bead diameter and sample thickness were pro-  
 196 cessed; see Tab. I and Fig. 2(a). Bead diameters were provided by the manufacturer and  
 197 are sufficiently accurate for long wavelength acoustical purposes.

TABLE I. Definition of the experimental samples.

Parameter	Sample #									
	R1	R2	R3	R4	R5	R6	R7	R8	R9	R10
Diameter, $d$ [mm]	3	4	5	6	7	3	4	5	6	7
Thickness, $L$ [mm]	23.5	23.5	23.5	23.5	23.5	47	47	47	47	47

198  
 199

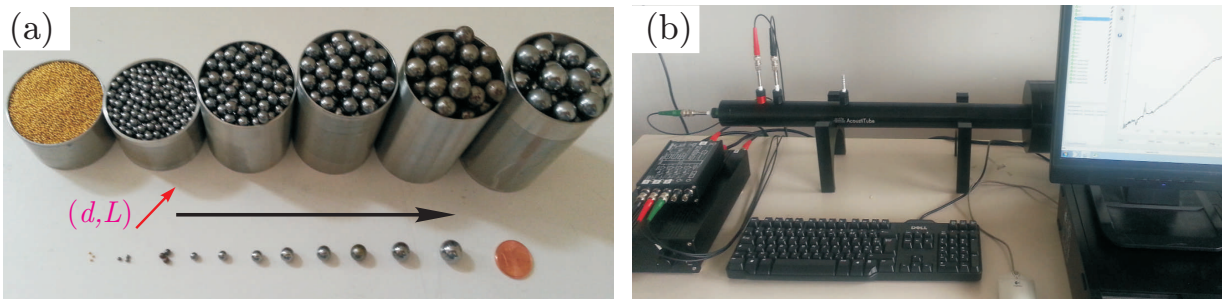


FIG. 2. (a) Samples of randomly-packed rigid spherical beads. The top row corresponds to sphere layers with a thickness of 47 [mm], while the bottom row shows 23.5 [mm]-thick layers. (b,c) Acoustical measurement setup and impedance tube configuration. Note that the specimen is backed by a rigid wall.

200 A two-microphone method was used to estimate the sound absorption coefficient of the  
 201 porous media at normal incidence, by measuring the pressure transfer function  $H_{12} = p_1/p_2$ ,

202 in which  $p_1$  and  $p_2$  are the pressures determined at the two microphones; see Fig. 2(b-c).  
 203 A steel net is used to control the sample thickness, see Fig. 2c. It is worth noticing that  
 204 manual measurements of the sample packing fraction can be expected to be less precise for  
 205 large bead diameters. The sound absorption coefficient is then experimentally estimated as

$$\alpha^{\text{exp}} = 1 - \left| \frac{\exp(jk_a d_{12}) - H_{12}}{H_{12} - \exp(-jk_a d_{12})} \exp(2jk_a L) \right|^2, \quad (14)$$

206 in which  $k_a$  represents the wavenumber in the ambient fluid,  $L$  is the sample thickness,  
 207 and  $d_{12}$  is the distance between microphones 1 and 2. Note that a third microphone at  
 208 the back of the sample could be used for accessing the intrinsic material properties such as  
 209 the wavenumber and the characteristic impedance by measuring a second pressure transfer  
 210 function  $H_{23} = p_2/p_3$ , in which  $p_3$  is the pressure measured at the third microphone<sup>32,33</sup> (see  
 211 Eqs. (1)–(4) in Ref.<sup>33</sup>). Measurements were conducted with an impedance tube of length 1  
 212 [m] and inner diameter 40 [mm] (see Fig. 2b), in the frequency range [100, 4500] [Hz] with  
 213 a sampling step of 4 [Hz]. The experimental results are reported in Fig. 3.

214 The normal incidence sound absorbing behavior of monodisperse spherical particles has  
 215 been discussed elsewhere; see Ref.<sup>34</sup>, Sec. VIII (and Refs.<sup>35,36</sup>) for instance. Indeed, it  
 216 was shown that accurate predictions of the first sound absorption peak can be obtained in  
 217 terms of frequency and magnitude from the geometrical properties of the material ( $d, L$ ).  
 218 The first normal incidence sound absorption peak corresponds to the quarter wavelength  
 219 resonant absorption of the material and is governed by its intrinsic damped wavelength  
 220  $\lambda_{eq}$  (and not directly by the wavelength in the air). The successive maxima appear at  
 221 the quarter wavelength, where  $L/\Re(\lambda_{eq}) = n/4$ , with  $n$  being successive odd integers. The  
 222 thickness-to-particle-diameter ratio  $L/d$  controls the magnitude of the first sound absorption

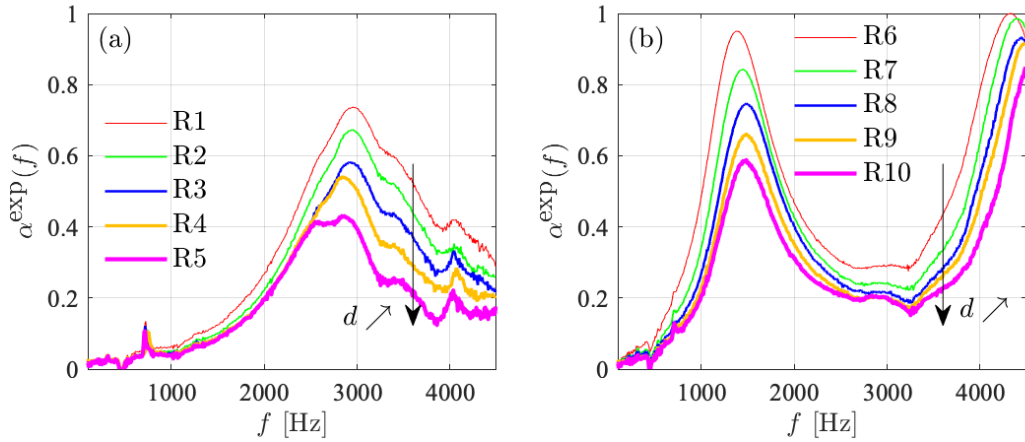


FIG. 3. Experimentally-measured sound absorption coefficients estimated for the samples described in Tab I.

223 peak, and the optimal value of the thickness-to-particle-diameter ratio  $N_{opt}$  allowing 100%  
 224 absorption at a given particle diameter was found to be a linear function of the particle  
 225 diameter (see Fig. 12 and Eq. (35) of Ref.<sup>34</sup>). Our experimental results are consistent with  
 226 the systematic analysis proposed in Ref.<sup>34</sup>, in which the optimal particle diameter is given,  
 227 for a given thickness  $L$ , as  $d_1(L) = \sqrt{L/\delta_1}$  (with  $\delta_1 = 12494$  [m<sup>-1</sup>]; see Ref.<sup>34</sup>). Note that  
 228 symbols  $d_1$  and  $\delta_1$  are used hereinafter for consistency with Ref.<sup>34</sup>. For the two considered  
 229 layer thicknesses, optimal particle diameters are estimated as  $d_1(L = 23.5$  [mm]) = 1.4 [mm]  
 230 and  $d_1(L = 47$  [mm]) = 1.9 [mm]. This explains why the sound absorption magnitude of  
 231 sample R6 reaches a maximum value above 0.9, whereas the first peak magnitude of sample  
 232 R1 is much lower than this critical value—even if the two samples involve the same particle  
 233 diameter,  $d = 2$  [mm]. The information described above constitutes the dataset for the  
 234 experimental response  $\boldsymbol{\mu} \mapsto \{\alpha^{\text{exp}}(\omega; \boldsymbol{\mu}), \omega \in \mathbb{W}\}$ , with  $\boldsymbol{\mu} = (d, L)^T$ .



235 **B. Multiscale surrogate**

236 We now introduce the computational surrogate for the experiments described in Sec.  
 237 [III A](#). Additional results pertaining to code verification and model accuracy are reported in  
 238 [Appendix A](#).

239 *1. Microstructural sampling*

240 The first step consists in sampling a random close packing of mono-sized rigid spheres  
 241 (for a given value of  $\mu$ ). To that aim, we rely on the algorithm proposed in Refs.<sup>37,38</sup> where  
 242 spheres are randomly distributed within the domain at initialization and moved, in an  
 243 iterative manner, to avoid overlaps and reach a target packing fraction. In order to enforce  
 244 a periodic structure at the boundaries of the simulation domain, each sphere intersecting  
 245 with  $p$  faces at the boundary ( $1 \leq p \leq 3$ ) is duplicated  $p$  times, and the center of each  
 246 replicate is translated towards the face opposing the intersecting boundary by a factor equal  
 247 to the size of the domain.<sup>39</sup> Four sphere ensembles with a target solid volume fraction of  
 248 0.6 are shown in [Fig. 4](#), for the sake of illustration. The radial distribution function  $g$  for  
 249 several packing configurations is shown in [Fig. 5](#). The generation of a microstructure with  
 250  $N = 128, 512, \text{ and } 1024$  spheres took about 35, 255, and 1523 [sec], respectively, on a laptop  
 252 equipped with an Intel(R) Core(TM) i7-4500U cadenced at 2.40 GHz.  
 253

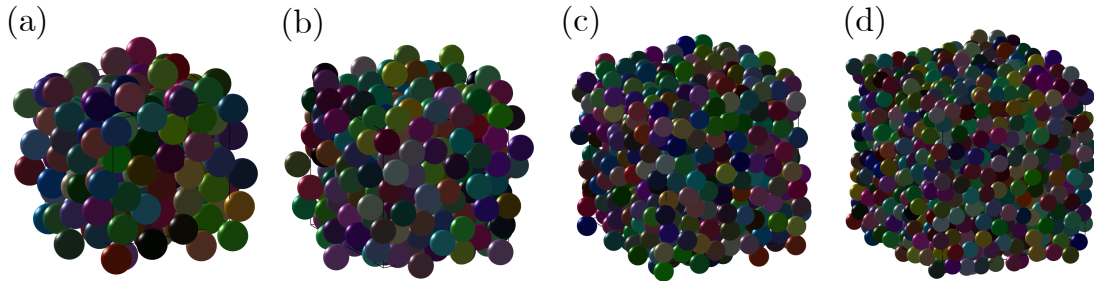


FIG. 4. Realizations of the random close packing obtained for  $N = 128$ ,  $N = 256$ ,  $512$ , and  $N = 1024$  (from left to right), for a solid volume fraction set to  $0.6$ .

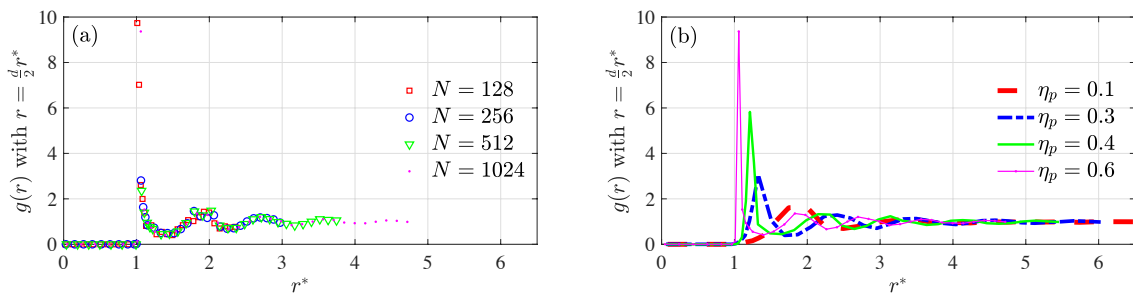


FIG. 5. Graph of the function  $g(r) \rightarrow r^*(= 2r/d)$  for: (a) various numbers  $N$  with a value of solid volume fraction  $\eta_p = 0.60$ , and (b) several packing fractions  $\eta_p$  with  $N = 1024$ .

## 254 **2. Determination of the transport properties**

255 The second step involves the calculation of transport properties using the periodic solid  
 256 skeleton defined in Sec. III B 1.

257 Let  $\Omega$  be the reconstructed Representative Volume Element (RVE) under consideration  
 258 with boundary  $\partial\Omega$ , and let its solid phase, fluid, and fluid-solid interface be denoted by  
 259  $\Omega_s$ ,  $\Omega_f$ , and  $\partial\Omega_f$ , respectively. The porosity (or fluid volume fraction)  $\phi$  and the thermal

260 characteristic length (or generalized hydraulic radius)  $\Lambda'$  are directly obtained as

$$\phi = \frac{\int_{\Omega_f} dV}{\int_{\Omega} dV}, \quad \Lambda' = 2 \frac{\int_{\Omega_f} dV}{\int_{\partial\Omega_f} dS}. \quad (15)$$

261 The macroscopic transport properties can be computed from the numerical solutions of a  
 262 series of canonical boundary value problems, namely: (i) a viscous flow problem, for the static  
 263 viscous permeability  $k_0$  and static viscous tortuosity  $\alpha_0$ ;<sup>5,7,8,40</sup> (ii) an inertial flow problem,  
 264 for the viscous characteristic length  $\Lambda$  and the high frequency tortuosity  $\alpha_\infty$ ;<sup>5,41,42</sup> and (iii)  
 265 a steady-state heat conduction problem, enabling for the static thermal permeability  $k'_0$  and  
 266 the static thermal tortuosity  $\alpha'_0$  to be computed.<sup>7,9,43</sup> These boundary value problems are  
 267 recalled below for the sake of self-containedness; interested readers are referred to<sup>19,40,44,45</sup>  
 268 for the first-principles calculations of these transport properties.

269 *a. Viscous flow.* This problem corresponds to the low frequency limit (that is, when  
 270  $\omega \rightarrow 0$ ) where viscous effects dominate, hence creating a steady-state flow in the porous  
 271 media. The flow, associated with an incompressible Newtonian fluid at very low Reynolds  
 272 numbers, is described by the scaled Stokes problem:<sup>40</sup>

$$-\nabla^2 \mathbf{k}_0^* + \nabla \pi_0^* = \mathbf{e}, \quad \nabla \cdot \mathbf{k}_0^* = 0 \quad (16)$$

273 in  $\Omega_f$ , with  $\mathbf{k}_0^* = \mathbf{0}$  on  $\partial\Omega_f$  and where the scaled velocity  $\mathbf{k}_0^*$  and pressure  $\pi_0^*$  of the fluid are  
 274  $\Omega$ -periodic. Here,  $\mathbf{e}$  is a unitary vector corresponding to the imposed macroscopic pressure  
 275 gradient that drives the flow in a preferential direction. The symbol  $\nabla$  denotes the nabla  
 276 differential operator, while “ $\cdot$ ” denotes the classical inner product in  $\mathbb{R}^3$ . The separation of  
 277 scales (and thereby, macroscopic isotropy) is assumed for the considered microstructure.<sup>?</sup>  
 278 The static viscous permeability  $k_0$  and the static viscous tortuosity  $\alpha_0$  are then calculated

279 as<sup>44,45</sup>

$$k_0 = \phi \langle \mathbf{k}_0^* \cdot \mathbf{e} \rangle, \quad \alpha_0 = \frac{\langle \mathbf{k}_0^* \cdot \mathbf{k}_0^* \rangle}{\langle \mathbf{k}_0^* \rangle \cdot \langle \mathbf{k}_0^* \rangle}, \quad (17)$$

280 where  $\langle \bullet \rangle$  indicates spatial averaging over the fluid domain. Notice that the aforementioned  
 281 scalar transport parameters are sufficient to describe the (isotropic) static viscous perme-  
 282 ability and tortuosity tensors.

283 *b. Inertial flow.* This problem is associated with the high-frequency regime,  $\omega \rightarrow +\infty$ .  
 284 In this case, inertial forces dominate over viscous ones and consequently, the saturating  
 285 fluid tends to behave as a nearly perfect fluid (without viscosity except in the vicinity of the  
 286 boundary layer). The inertial flow of the perfect incompressible fluid then formally behaves  
 287 according to an electric conduction phenomenon (where the porous material is composed  
 288 of a non-conducting solid matrix and a conducting fluid).<sup>5,41,42</sup> Quantities of interest in the  
 289 inertial flow problem can be thus obtained by solving the following set of potential equations:

290

$$\mathbf{E} = -\nabla\varphi + \mathbf{e}, \quad \nabla \cdot \mathbf{E} = 0 \quad (18)$$

291 in  $\Omega_f$ , subjected to  $\mathbf{E} \cdot \mathbf{n} = 0$  on  $\partial\Omega_f$  and  $\varphi$  is  $\Omega$ -periodic. In the above equations,  $\mathbf{e}$  is a  
 292 given macroscopic electric field,  $\mathbf{E}$  is the local solution to the boundary value problem having  
 293  $-\nabla\varphi$  as a fluctuating part, and  $\mathbf{n}$  is the unit normal to  $\partial\Omega_f$ . The viscous characteristic  
 294 length  $\Lambda$  and the through-thickness high-frequency tortuosity  $\alpha_\infty$  are given by<sup>5,46</sup>

$$\Lambda = 2 \frac{\int_{\Omega_f} \mathbf{E} \cdot \mathbf{E} dV}{\int_{\partial\Omega_f} \mathbf{E} \cdot \mathbf{E} dS}, \quad \alpha_\infty = \frac{\langle \mathbf{E} \cdot \mathbf{E} \rangle}{\langle \mathbf{E} \rangle \cdot \langle \mathbf{E} \rangle}. \quad (19)$$

295 Similarly to the static viscous permeability and tortuosity parameters introduced in the pre-  
 296 vious section, these scalar quantities are sufficient to parameterize the homogenized response  
 297 of the material (owing to macroscopic isotropy).

298 *c. Thermal effects.* In the low frequency limit (that is, in the static case), heat diffusion  
 299 in porous media is governed by the Poisson equation<sup>43</sup>

$$\nabla^2 \tau = -1 \quad (20)$$

300 in  $\Omega_f$ , with  $\tau = 0$  on  $\partial\Omega_f$  and  $\tau$  is  $\partial\Omega$ -periodic. The static thermal permeability  $k'_0$  and  
 301 static thermal tortuosity  $\alpha_\infty$  are finally estimated as<sup>41</sup>

$$k'_0 = \langle \tau \rangle, \quad \alpha'_0 = \frac{\langle \tau^2 \rangle}{\langle \tau \rangle^2}. \quad (21)$$

302 As an illustration, Figure 6 shows the solution fields obtained by the finite element method  
 303 (with a  $\mathbb{P}_2 - \mathbb{P}_1$  formulation) for a cubic domain of edge length  $2.5d$ .

### 305 *3. Determination of the sound absorption coefficient*

306 Within the framework of the equivalent-fluid theory,<sup>46</sup> the air in a porous medium is  
 307 replaced by an equivalent fluid that exhibits (i) the same bulk modulus as the saturating air,  
 308 and (ii) a dynamic density that takes into account the viscous and the inertial interactions  
 309 with the frame. The determination of these two dynamic parameters subsequently enables  
 310 the estimation of the the wavenumber and characteristic impedance, which in turn can  
 311 be used to define some relevant properties of the air-filled porous media. In the JCAPL  
 312 model,<sup>5,6,9</sup> developed following this macroscopic perspective, the effective density and the

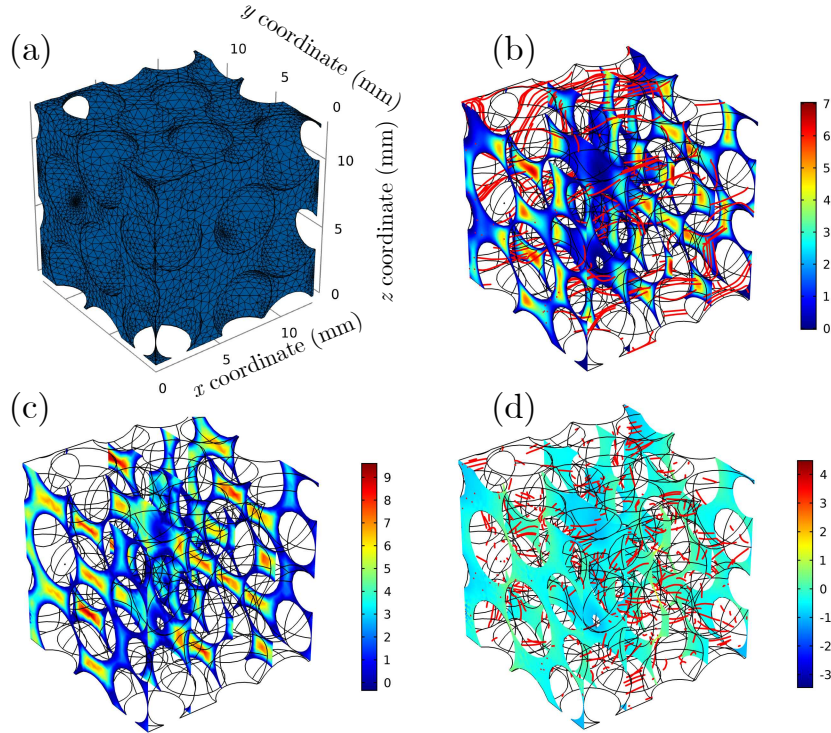


FIG. 6. Asymptotic solution fields: (a) mesh containing 58 400 Lagrangian tetrahedral elements; (b) low-frequency scaled velocity field  $\mathbf{k}_0^*$  [ $\times 10^{-8}$  m<sup>2</sup>]; (c) low-frequency scaled temperature field  $\tau$  [ $\times 10^{-8}$  m<sup>2</sup>]; (d) high-frequency scaled velocity field  $\mathbf{E}$  [-] for an external unit field  $\mathbf{e}$ ;

313 effective bulk modulus are respectively defined as

$$\tilde{\rho}(\omega) = \frac{\rho_0 \tilde{\alpha}(\omega)}{\phi}, \quad \tilde{K}(\omega) = \frac{\gamma P_0}{\phi} \frac{1}{\tilde{\beta}(\omega)}, \quad (22)$$

314 where  $\rho_0$  is the density of the saturating fluid (here, the air),  $\gamma = C_p/C_v$  where  $C_p$  is  
 315 the pressure volume-specific heat and  $C_v$  is the constant pressure-specific heat,  $P_0$  is the  
 316 atmospheric pressure, and  $\phi$  is the open porosity. The dynamic tortuosity and dynamic  
 317 compressibility, denoted by  $\tilde{\alpha}(\omega)$  and  $\tilde{\beta}(\omega)$  respectively, are then evaluated as

$$\tilde{\alpha}(\omega) = \left[ 1 + \frac{1}{j\varpi'} \tilde{F}(\omega) \right], \quad \tilde{\beta}(\omega) = \gamma - (\gamma - 1) \left[ 1 + \frac{1}{j\varpi'} \tilde{F}'(\omega) \right]^{-1}, \quad (23)$$

318 where  $j$  is the imaginary unit,  $\tilde{F}(\omega)$  and  $\tilde{F}'(\omega)$  are the dimensionless viscous and thermal  
 319 shape functions depending on the dimensionless viscous and thermal angular frequencies  
 320 (denoted by  $\varpi$  and  $\varpi'$ , respectively), defined as

$$\tilde{F}(\omega) = 1 - P + P\sqrt{1 + \frac{M}{2P^2}j\varpi}, \quad \tilde{F}'(\omega) = 1 - P' + P'\sqrt{1 + \frac{M'}{2P'^2}j\varpi'}, \quad (24)$$

321 with

$$\varpi = \omega \frac{\rho_0 k_0 \alpha_\infty}{\phi \eta}, \quad \varpi' = \omega \frac{k'_0 \rho_0 C_p}{\phi \gamma P_0}. \quad (25)$$

322 The four non-dimensional shape factors  $M$ ,  $M'$ ,  $P$ , and  $P'$  only depend on the material  
 323 transport parameters introduced in Sec. III B 2:

$$M = \frac{8\alpha_\infty}{k_0 \Lambda^2 \phi}, \quad P = \frac{M}{4(\alpha_0/\alpha_\infty - 1)}, \quad M' = \frac{8k'_0}{\Lambda'^2 \phi}, \quad P' = \frac{M'}{4(\alpha'_0 - 1)}. \quad (26)$$

324 It should be noticed that the so-called Johnson-Champoux-Allard (JCA) and Johnson-  
 325 Champoux-Allard-Lafarge (JCAL) models are recovered by letting  $M' = P = P' = 1$   
 326 and  $P = P' = 1$ , respectively.

327 For a homogeneous acoustic layer, the wavenumber  $\tilde{k}(\omega)$  and the characteristic impedance  
 328  $\tilde{Z}_c(\omega)$  can be calculated by

$$\tilde{k}(\omega) = \omega \sqrt{\frac{\tilde{\rho}(\omega)}{\tilde{K}(\omega)}}, \quad \tilde{Z}_c(\omega) = \sqrt{\tilde{\rho}(\omega) \tilde{K}(\omega)}. \quad (27)$$

329 In the third and final step, the sound absorption coefficient at normal incidence of the  
 330 absorbing porous layer backed by a rigid wall is defined as

$$\alpha^{\text{sim}}(\omega) = 1 - \left| \frac{\tilde{Z}_s(\omega) - Z_0}{\tilde{Z}_s(\omega) + Z_0} \right|^2, \quad (28)$$

331 where  $Z_0$  is the characteristic impedance of ambient air and  $\tilde{Z}_s(\omega) = -j\tilde{Z}_c(\omega)\cot[\tilde{k}(\omega)L]$  is  
 332 the surface impedance on the free face of the sample having thickness  $L$ .

333 **4. Numerical results**

334 The entire set of transport parameters for the sphere-packing microstructure is reported  
 335 in Tab. II for the specific case  $d = 5$  [mm]. These parameters provide information relevant

TABLE II. Transport properties computed for  $d = 5$  [mm].

$\phi$ [-]	$\Lambda'$ [mm]	$\Lambda$ [mm]	$k_0$ [ $\times 10^{-8}$ m <sup>2</sup> ]	$k'_0$ [ $\times 10^{-8}$ m <sup>2</sup> ]	$\alpha_\infty$ [-]	$\alpha_0$ [-]	$\alpha'_0$ [-]
0.37	0.97	0.70	1.75	2.56	1.46	2.29	1.67

336

337

338 to the propagation and dissipation phenomena in the equivalent homogeneous material, in  
 339 accordance with the multiscale setting, and allows one to estimate the sound absorption  
 340 coefficient  $\alpha(\omega)$  (following the derivations in the previous sections).

341 In order to build the mapping  $\boldsymbol{\mu} \mapsto \{\alpha^{\text{sim}}(\omega; \boldsymbol{\mu}), \omega \in \mathbb{W}\}$ , samples of  $\boldsymbol{\mu}$  are drawn from  
 342 the product of uniform probability measures on the intervals [1, 10] [mm] (for the diameter  
 343  $d$ ) and [5, 100] [mm] (for the sample thickness  $L$ ). Note that these intervals are relevant to  
 344 a broad range of absorber configurations, as discussed in Ref.<sup>34</sup>. Results obtained for the  
 345 ten configurations defined in Tab. III are displayed in Fig. 7.

346 **C. Deploying the methodology**

347 For numerical purposes, we consider discretized expansions associated with a frequency  
 348 step of 4 [Hz]. Notice that the results reported in this section are displayed in terms of  
 349 frequency  $f$ .



TABLE III. List of parameters for the virtual sphere-packing samples analyzed in Fig. 7.

Parameter	Sample name									
	V1	V2	V3	V4	V5	V6	V7	V8	V9	V10
Diameter, $d$ [mm]	5.24	3.07	8.60	2.75	3.03	2.54	3.05	4.92	3.79	9.31
Thickness, $L$ [mm]	93.24	74.38	51.42	59.96	27.54	48.59	96.49	56.95	54.51	27.00

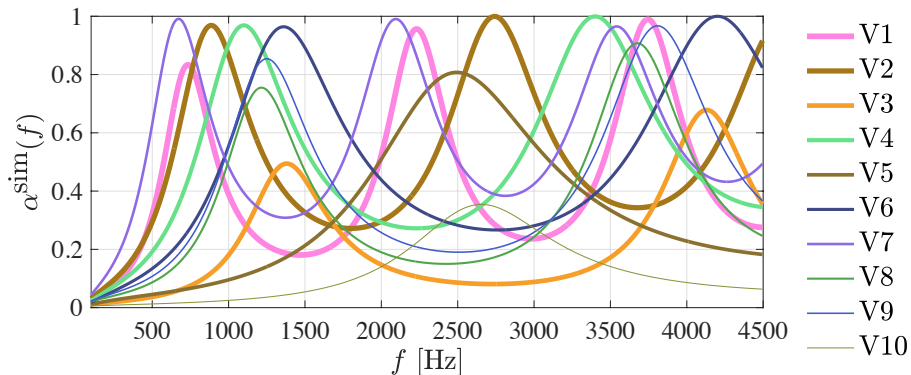


FIG. 7. Predicted sound absorption coefficients for the ten virtual samples described in Tab. III.

### 350 1. Statistical reduction for the computational surrogate

351 The first step of the methodology consists in analyzing the reduction of the process  
352  $\{\alpha^{\text{sim}}(\omega), \omega \in \mathbb{W}\}$ , based on a set of samples of  $\boldsymbol{\mu}$ . To identify the number of realizations that  
353 are necessary to achieve convergence for the projection basis, we characterize the convergence  
354 of the statistical estimator for the covariance matrix of the discretized process, denoted  
355 by  $[\tilde{C}]$ . The graph of the function  $N^{\text{sim}} \mapsto \|[\tilde{C}(N^{\text{sim}})]\|$  is shown in Fig. 8, where  $N^{\text{sim}}$

356 denotes the number of realizations used to compute the estimator. It is seen that reasonable

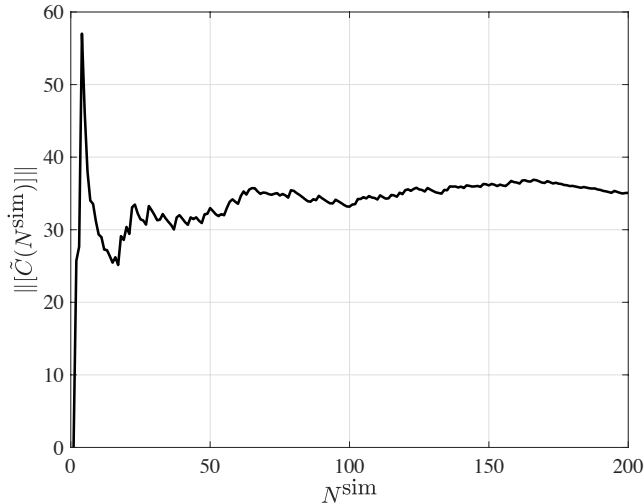


FIG. 8. Graph of the Frobenius norm of the statistical estimator for the covariance matrix, as a function of the number of samples  $N^{\text{sim}}$ . This figure shows that 200 samples are sufficient to compute  $[\tilde{C}]$ .

357  
358

359 convergence is achieved for  $N^{\text{sim}} = 200$ , which is the number considered in subsequent  
360 calculations.

361 We next determine the truncation order  $\nu$  in the statistical reduction (see Eq. (5)) by  
362 analyzing the convergence of the function  $m \mapsto \text{Err}(m)$  defined as

$$\text{Err}(m) = 1 - \frac{\sum_{i=1}^m \lambda_i^{\text{sim}}}{\text{tr}([\tilde{C}])}. \quad (29)$$

363 The graph of the error function is shown in Fig. 9. It is found that the error is less than  
365  $1 \times 10^{-2}$  (respectively  $1 \times 10^{-4}$  and  $1 \times 10^{-6}$ ) for  $m = 10$  (respectively  $m = 21$  and  $m = 33$ ).

366 The graphs of the first five eigenfunctions  $\{\omega \mapsto \varphi_i^{\text{sim}}(\omega)\}_{i=1}^5$  are displayed in Fig. 10. In what  
368 follows, we consider a truncation at order  $\nu = 21$ , and a quantitative comparison between the

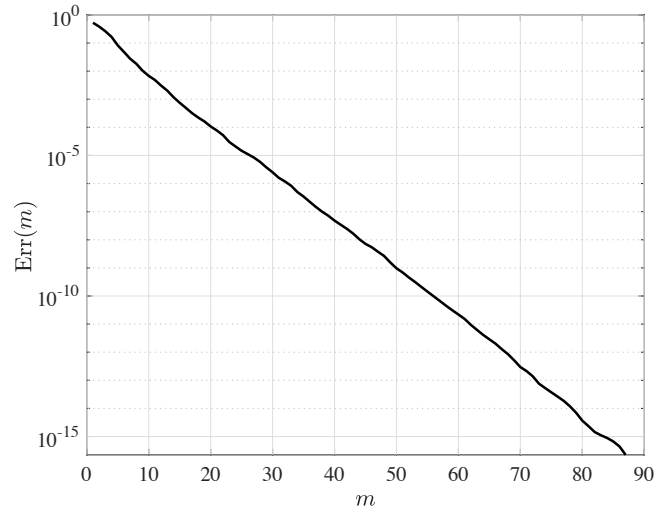


FIG. 9. Graph of the function  $m \mapsto \text{Err}(m)$  measuring the error induced by the truncation in the KL decomposition.

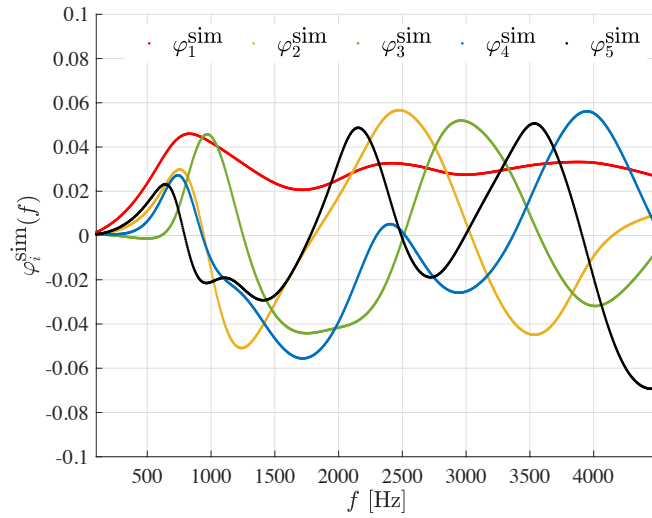


FIG. 10. Graph of the five first eigenfunctions which are used to represent the sound absorption coefficient obtained from the multiscale formulation.

369 reference sound absorption coefficient  $\alpha^{\text{sim}}$  and the truncated KL representation is provided  
 370 in Fig. 11, for a specific microstructural sample.

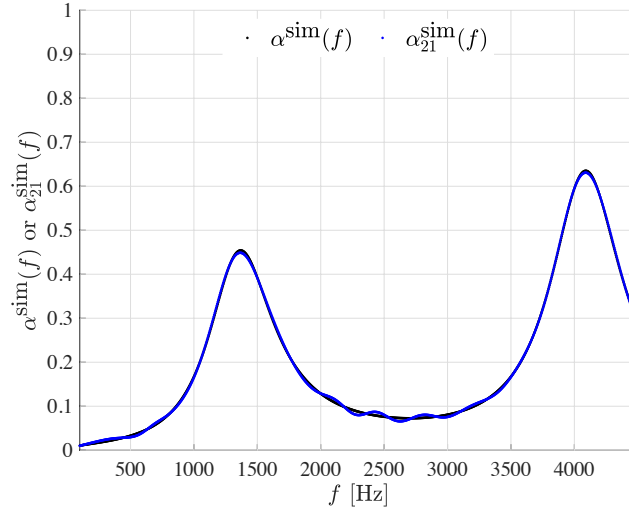


FIG. 11. Graphs of the reference function  $f \mapsto \alpha^{\text{sim}}(f)$  (black dots) and approximation  $f \mapsto \alpha_{21}^{\text{sim}}(f)$  for a truncation order  $\nu = 21$  (blue dots) for the virtual sample with  $d = 9.61$  [mm] and  $L = 52.00$  [mm].

371

372

## 373 2. Neural network surrogate for the computational reduced coordinates

374 Following the second step in the approach outlined in Sec. II A, samples for the reduced  
 375 coordinates associated with the multcale computational model are obtained as

$$\eta_i^{\text{sim}}(\mathbf{m}) = \frac{1}{\sqrt{\lambda_i^{\text{sim}}}} \langle \alpha^{\text{sim}}(\bullet; \mathbf{m}) - \underline{\alpha}^{\text{sim}}, \varphi_i^{\text{sim}} \rangle, \quad (30)$$

376 where  $\mathbf{m}$  denotes a realization of  $\boldsymbol{\mu}$ , and the mapping  $\boldsymbol{\mu} \mapsto \boldsymbol{\eta}^{\text{sim}}(\boldsymbol{\mu})$  is approximated by using  
 377 a neural network (with  $\mathcal{I} = 2$  and  $\mathcal{O} = 21$ , following the notation introduced in Sec. II B 1).

378 As previously indicated, a feed forward NN is used in this work, and the architecture was  
 379 determined through a parametric analysis in terms of  $N_H$  (number of hidden layers) and the  
 380 set  $\{n_\ell\}_{\ell=1}^{N_H}$  (number of neurons per layer, for all layers). While no attempt was made to fully  
 381 optimize the architecture for the problem at hand, a structure with 5 hidden layers and  $\nu$ ,  $3\nu$ ,  
 382  $\nu$ ,  $\nu$ , and  $\nu$  neurons per layer, respectively, was found to provide reasonably accurate results  
 383 (recall that  $\nu = 21$ ). The convergence of the mean squared error for the training, validation,  
 384 and testing stages can be seen in Fig. 14. Here, the training, validation, and testing sets  
 385 were composed of 144, 18, and 18 samples, respectively. The prediction obtained by using

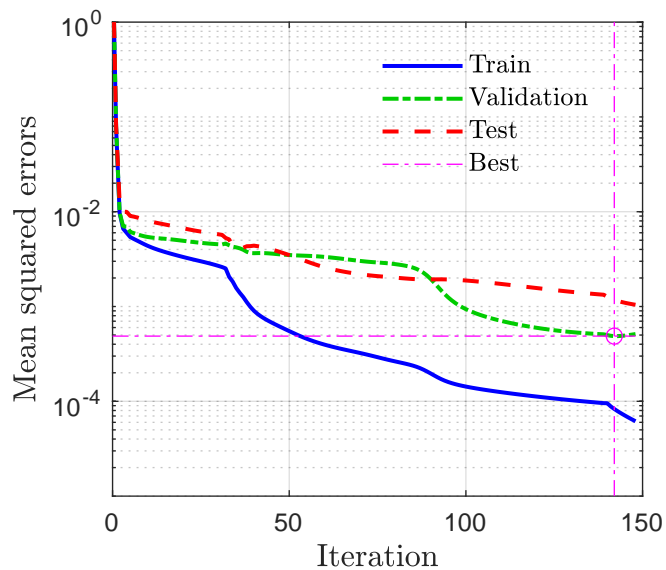


FIG. 12. Performance of the proposed NN model within the numerical training dataset: Convergence of the mean squared errors for training, validation, and testing, respectively.

386

387

388 the NN surrogate with the truncated (KL) expansion for a given sample (not considered  
 389 during the training process) can be seen in Fig. 13. It is seen that the surrogate predicts the  
 391 sound absorption response fairly accurately over the whole frequency domain for the virtual

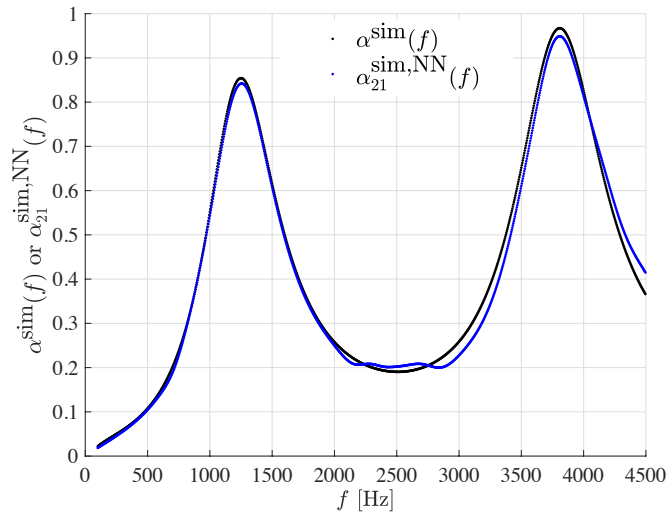


FIG. 13. Graphs of the reference function  $f \mapsto \alpha^{\text{sim}}(f)$  (black dots) and approximation  $f \mapsto \alpha_{21}^{\text{sim,NN}}(f)$  defined through the KL expansion ( $\nu = 21$ ) and the NN model (blue dots) for the virtual sample with  $d = 3.8$  [mm] and  $L = 54.51$  [mm].

392 sample under consideration. In particular, the location and magnitude of the peaks are well  
 393 estimated. It should, however, be pointed out that larger (but still contained) discrepancies  
 394 can be observed on some other samples. The observed errors stem from the combination of  
 395 the error raised by the truncation in the KL expansion, which can be reduced by increasing  
 396  $\nu$ , and the error generated by the NN surrogate, which may be decreased by refining the  
 397 architecture and training strategy.

398 **3. Neural network surrogate for the experimental reduced coordinates and exper-**  
 399 **imental sound absorption prediction**

400 In the final step of the methodology, transfer learning is applied to approximate the  
 401 mapping  $\boldsymbol{\mu} \mapsto \hat{\boldsymbol{\eta}}^{\text{exp}}(\boldsymbol{\mu})$  with the limited dataset (composed of only 10 samples). To this end,  
 402 a shallow network is added to the neural network constructed and calibrated in Sec. III C 2,  
 403 with the aim of representing the mapping  $\boldsymbol{\eta}^{\text{sim}} \mapsto \hat{\boldsymbol{\eta}}^{\text{exp}}$ . The additional layer contains  $\nu$   
 404 neurons, and is also optimized with the Levenberg-Marquardt algorithm. Results from the  
 405 training, validation, and testing stages are reported in Fig. 14. A small number of epochs

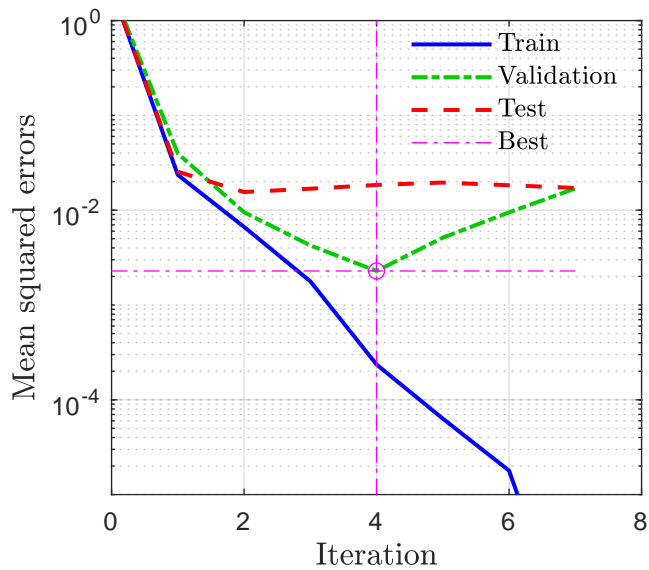


FIG. 14. Performance of the proposed NN model within the experimental dataset: Convergence of the mean squared errors for training, validation, and testing, respectively.

406  
 407

408 is necessary to obtain good approximation results in the transfer learning approach, which  
 409 suggests that the computational surrogate is fairly accurate. The increase of the mean  
 410 squared error for the validation test suggests overfitting, which may be alleviated through

411 various strategies including model simplification, regularization (with early stopping, for  
 412 instance), and noise addition to list a few. As stated earlier, no attempt was made to  
 413 optimize the machine learning part of the framework, given the scope of this study, and  
 414 refinements along those lines are left for future work.

415 Finally, the experimental sound absorption coefficient is predicted as

$$\alpha_\nu^{\text{exp,NN}}(\omega) = \underline{\alpha}^{\text{exp}}(\omega) + \sum_{i=1}^{\nu} \sqrt{\lambda_i^{\text{sim}}} \hat{\eta}_i^{\text{exp,NN}} \varphi_i^{\text{sim}}(\omega), \quad (31)$$

416 where  $\hat{\eta}^{\text{exp,NN}}$  denotes the neural network surrogate calibrated through transfer learning.  
 417 The graphs of the experimentally-measured sound absorption coefficient  $\alpha^{\text{exp}}$  and the pre-  
 418 diction  $\alpha_\nu^{\text{exp,NN}}$  for the physical samples R3 and R7 (see Tab. I), which were both discarded  
 419 for training, are shown in Figs. 15 and 16, respectively. It is seen that the hybrid surrogate

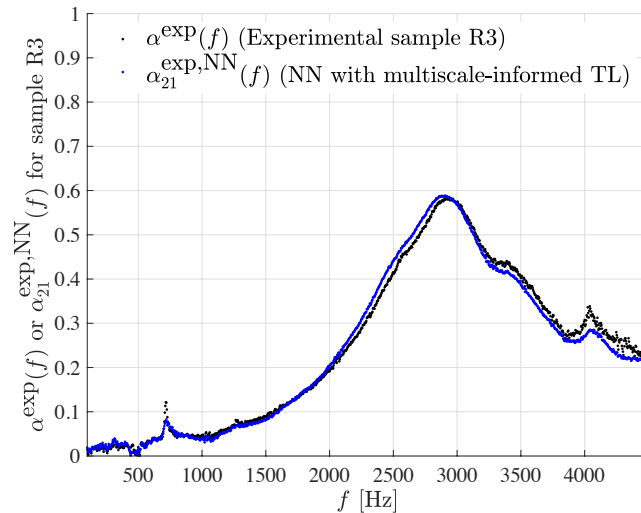


FIG. 15. Graphs of the experimentally-measured sound absorption coefficient  $\alpha^{\text{exp}}$  and neural network prediction  $\alpha_{21}^{\text{exp,NN}}$  for sample R3 (see Tab. I).

420

422

423 model combining the KL expansion with the computationally-based projection basis and



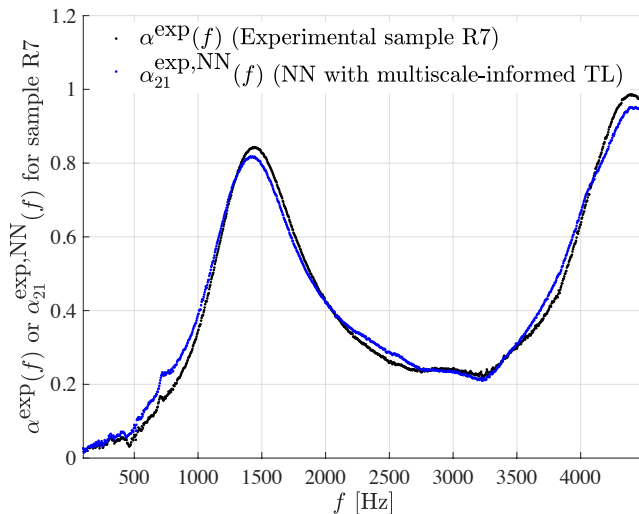


FIG. 16. Graphs of the experimentally-measured sound absorption coefficient  $\alpha^{\text{exp}}$  and neural network prediction  $\alpha_{21}^{\text{exp,NN}}$  for sample R7 (see Tab. I).

424 the neural network calibrated through transfer learning predicts the experimental responses  
 425 very well, even if only 8 experimentally-characterized samples were used as the dataset.  
 426 While the responses for R3 and R7 remain quite different from one another, the surrogate  
 427 can properly estimate the locations of small and large peaks, as well as the corresponding  
 428 magnitudes in both cases. In practice, a normalized  $L^2$  error, defined as

$$\varepsilon_\nu = \frac{\|\alpha^{\text{exp}} - \alpha_\nu^{\text{exp,NN}}\|}{\|\alpha^{\text{exp}}\|}, \quad (32)$$

429 can be used to assess the accuracy of the prediction. This error is equal to 5.4% and 5.7%  
 430 for samples R3 and R7, respectively. Other analyses (which are not reported below for the  
 431 sake of conciseness) were performed by using other pairs of discarded responses (in lieu of  
 432 R3 and R7), and similar results were obtained regarding the quality of the approximations.  
 433 It should be noticed that the asymptotic result  $\lim_{\nu \rightarrow \infty} \varepsilon_\nu = 0$  holds in the big data limit

434 (which is not the setting considered in this paper), owing to the universal approximation  
435 theorem<sup>47,48</sup>. The rate of convergence depends on several factors, among which the accu-  
436 rary of the computational model, the architecture of the neural network, and the amount  
437 of experimental data available for transfer learning. It is also noteworthy that the sound  
438 absorbing spectrum obtained from the recorded time series (Fig. 3) showed significant dips  
439 (400 [Hz]) and peaks (700 [Hz]) of small amplitudes; similar features can also be seen in  
440 the frequency range [3000 – 4000] [Hz]. Figures 15 and 16 suggest that these inaccuracies  
441 originating presumably from the experimental setup and associated characterization method  
442 are also captured and reproduced by the neural network; meaning that the transfer learn-  
443 ing approach produces datasets consistent with experimental observations and quantified  
444 experimental uncertainties.

#### 445 IV. CONCLUSION

446 A novel methodology to learn acoustical responses based on limited experimental datasets  
447 was presented. From a methodological standpoint, the approach combines a multiscale-  
448 informed encoder, used to cast the learning task in a finite-dimensional setting, with a  
449 neural network model acting between the set of microstructural descriptors (comprised of  
450 the monodisperse particle diameter and the sample thickness in the presented application)  
451 and the reduced (latent) variables. The neural network is trained through transfer learn-  
452 ing, using synthesized multiscale data to compensate for experimental data scarcity. The  
453 relevance of the approach was investigated by considering the prediction of the sound ab-  
454 sorption coefficient. It was shown that the proposed strategy allows for the map between the

455 microstructural parameters and the acoustic response to be well approximated, even with  
456 limited data.

457 From an application standpoint, this work demonstrates how the experiments and models  
458 typically obtained and developed into several significant contributions to acoustics can be  
459 combined to enrich datasets in a context that many researchers in the field of acoustical  
460 materials encounter—namely, the identification and validation of models parameterized by  
461 micro-/structural features, based on a few experimental samples. The methodology allows  
462 one to explore these important aspects with the ability to account for microscopic effects,  
463 as well as correlation effects between local properties of the medium. It also paves the way  
464 for cost reduction through the efficient exploration of the parameter space for acoustical  
465 materials design.

466 Avenues for future research include refinements on the learning components such as net-  
467 work architecture and learning strategy, as well as the assessment of the methodology for  
468 other acoustical responses (e.g., intrinsic frequency-dependent properties of polydisperse  
469 granular structures).

## 470 **ACKNOWLEDGMENTS**

471 This work was funded by the Vietnam National Foundation for Science and Technology  
472 Development (NAFOSTED) under Grant Number 107.01-2019.316.

## 473 APPENDIX A: VALIDATION OF MULTISCALE-INFORMED PREDICTIONS

474 In this appendix, we report results pertaining to code verification and model valida-  
 475 tion. Alternative analytical models for transport parameters are first presented in Sec. A1.  
 476 Comparisons of multiscale-inferred estimations for the transport properties and the sound  
 477 absorption coefficient are then proposed in Secs. A2. and A3

### 478 1. Analytical models for transport properties

479 Several analytical models can be used for estimating the transport properties fed as  
 480 inputs for the JCAPL semi-phenomenological model. Here, we specifically consider three  
 481 models proposed in Refs. <sup>44,45</sup>, whose parameters are estimated as follows. The characteristic  
 482 lengths and permeabilities are defined by the equations listed in Tab. IV. Three cases are  
 483 considered, namely (i) the P-estimate (for which the shear stress vanishes at the boundary);  
 484 (ii) the V-estimate (for which tangential velocities are equal at the boundary); and (iii) the  
 485 C-estimate (with vanishing velocity at the boundary). The high-frequency tortuosity factor  
 486 is defined as  $\alpha_\infty = (3 - \phi)/2$  for all three cases. The static viscous tortuosities are estimated  
 487 for  $\phi = 0.37$  as  $\alpha_{0V} = 1.52$ ,  $\alpha_{0C} = 1.58$ , and  $\alpha_{0P} = 1.60$ . The static thermal tortuosity  $\alpha'_0$  is  
 488 finally equal to 1.94, in agreement with Ref. <sup>34</sup>.

### 489 2. Validation of the multiscale framework

490 Three classical cubic lattices are chosen for the sake of verification, namely simple cubic  
 492 (SC), body-centered cubic (BCC), and face-centered cubic (FCC) lattices; see Fig. 17. Here,

TABLE IV. Analytical estimates derived by combining periodic homogenization and the self-consistent scheme. The determination of the characteristic lengths and permeabilities of spherical packings is based on a bicomposite spherical pattern. Here,  $R = d/2\beta$  with  $\beta = \sqrt[3]{1-\phi}$ .<sup>45</sup>

Factor	Method		
	P-estimate	C-estimate	V-estimate
$\Lambda/R$	$\frac{2\phi(3-\phi)}{9(1-\phi)}$	$\frac{2\phi(3-\phi)}{9(1-\phi)}$	$\frac{2\phi(3-\phi)}{9(1+\beta^4)(1-\phi)}$
$\Lambda'/R$	$\frac{2\phi}{3(1-\phi)}$	$\frac{2\phi}{3(1-\phi)}$	$\frac{2\phi}{3(1-\phi)}$
$k_0/R^2$	$\frac{2-3\beta+3\beta^5-2\beta^6}{9\beta+6\beta^6}$	$\frac{10-18\beta+10\beta^3-2\beta^6}{45\beta}$	$\frac{4-9\beta+10\beta^3-9\beta^5+4\beta^6}{18(\beta^1-\beta^6)}$
$k'_0/R^2$	$\frac{3}{2\pi} \frac{10-18\beta+10\beta^3-2\beta^6}{45\beta}$	$\frac{3}{2\pi} \frac{10-18\beta+10\beta^3-2\beta^6}{45\beta}$	$\frac{3}{2\pi} \frac{10-18\beta+10\beta^3-2\beta^6}{45\beta}$

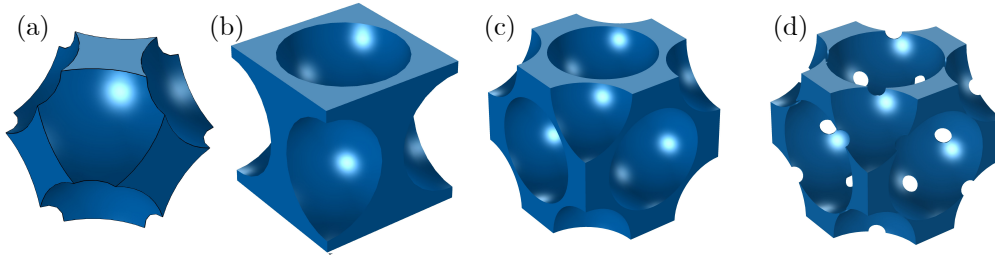


FIG. 17. Periodic unit cells of [SC (a), BCC (b), and FCC (c)] at  $\phi = 0.42$ , and FCC (d) at  $\phi = 0.26$  within solder joints with a radius of  $150 [\mu\text{m}]$ .<sup>49</sup>

493 the sphere radius is equal to 1 [mm] for all patterns. Computational results are compared  
 498 with those from Refs.<sup>50,51</sup> and are found to be in good agreement, see Tab. V. The evolution  
 496 of the sound absorption coefficient (at normal incidence) obtained from either the semi-

TABLE V. Numerical transport properties for classical lattices of spheres.

Lattice	Reference	Transport parameters							
		$\phi$	$\Lambda'$	$\Lambda$	$k_0$	$k'_0$	$\alpha_\infty$	$\alpha_0$	$\alpha'_0$
		[-]	[mm]	[mm]	$\times 10^{-10}$ [m <sup>2</sup> ]	$\times 10^{-10}$ [m <sup>2</sup> ]	[-]	[-]	[-]
SC	Ref. <sup>50</sup>	0.48	0.624	0.369	102	246	1.40	2.02	1.43
	Present		0.621	0.338	103	251	1.38	2.16	1.44
	Ref. <sup>51</sup>	0.42	1.56	0.99	535	1457	1.53	2.31	1.45
	Present		1.56	0.99	546	1459	1.53	2.31	1.44
BCC	Ref. <sup>50</sup>	0.32	0.325	0.234	19.7	38.1	1.48	2.15	1.35
	Present		0.319	0.189	21.1	37.9	1.47	2.22	1.39
	Ref. <sup>51</sup>	0.42	1.43	1.11	435	800	1.32	1.95	1.32
	Present		1.43	1.11	452	803	1.32	1.93	1.31
FCC	Ref. <sup>50</sup>	0.26	0.247	0.159	6.70	27	1.65	2.49	1.85
	Present		0.247	0.157	6.76	26.3	1.66	2.65	1.91
	Ref. <sup>51</sup>	0.42	1.43	1.12	365	817	1.32	1.86	1.55
	Present		1.42	1.12	393	834	1.32	1.84	1.52

phenomenological models (fed with transport parameters) or the direct numerical approach presented in Ref.<sup>49</sup> is shown in Fig. 18. The agreement between the different predictions

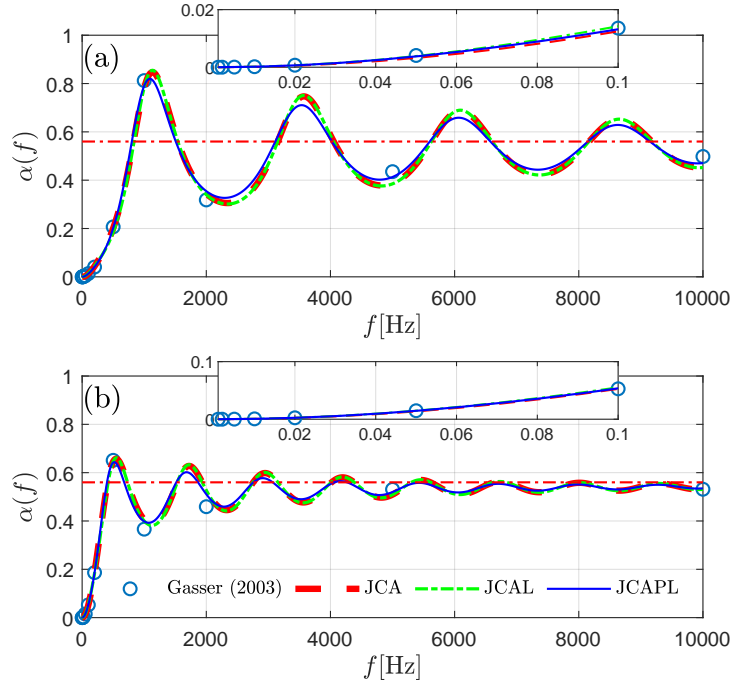


FIG. 18. Comparison of the normal incidence sound absorbing behavior obtained with the direct numerical method (circle markers) and a hybrid method based on the JCA model (dashed line), the JCAL model (dash-dotted line), and the JCAPL model (continuous line): (a)  $L = 50$  [mm] and (b)  $L = 100$  [mm]. The inset plots show the same information with a focus on low frequencies (smaller than 0.1 [kHz]). The horizontal dashed line is the high-frequency sound absorption limit  $\alpha_h = 0.56$  for the FCC pattern under study, at a porosity  $\phi = 0.26$ .

499  
500

shows that the hybrid approach allows the sound absorbing behavior to be well described. The absorbers are based on FCC packings (Fig. 17d) having two different thicknesses,  $L \in \{50, 100\}$  [mm]. The considered frequencies range between 1 to 10 000 [Hz]. In the direct approach, the SAC value is estimated from the effective factors  $\tilde{\rho}(\omega)$  and  $\tilde{\beta}(\omega)$  taken from

505 Tabs. 3.4 and 3.5 in Ref.<sup>49</sup>. In agreement with results published elsewhere,<sup>19,34,50</sup> the normal  
 506 incidence sound absorption coefficient of sphere-packed porous absorbers exhibits quarter-  
 507 wavelength resonances (see also Sec. IIIA), and oscillates around the high-frequency sound  
 508 absorption limit,  $\alpha_h = 1 - [(\hat{z} - 1)/(\hat{z} + 1)]^2$  with  $\hat{z} = \phi/\sqrt{\alpha_\infty}$ .<sup>52</sup>

### 509 3. Comparison of multiscale-informed sound absorption predictions

510 The predictions of the normal incidence SAC obtained from different approaches are  
 511 compared below. The experimentally-measured sound absorbing behavior of the ten real  
 512 samples introduced in Tab. I is compared with both simulations (combining the JCAPL  
 513 model with the finite element results on dense random packing of equal spheres) and ana-  
 514 lytical estimates (combining the JCAPL model with the self-consistent estimates described  
 515 in Sec. A1)<sup>44,45</sup>. In general, the hybrid multi-scale numerical approach is shown to provide  
 516 a fairly good estimate of the experimental behavior, as seen in Fig. 19. However, as the  
 517 particle diameter to sample thickness ratio increases (samples R4 and R5), border effects  
 518 become significant in the experimental response and a RVE model is less appropriate to  
 519 simulate such configurations (Fig. 19d and e).

### 521 References

522 <sup>1</sup>C. Zwikker and C. W. Kosten, *Sound absorbing materials* (Elsevier, 1949).

523 <sup>2</sup>M. A. Biot, “Theory of propagation of elastic waves in a fluid-saturated porous solid. I.  
 524 low-frequency range,” J. Acoust. Soc. Am. **28**(2), 168–178 (1956).



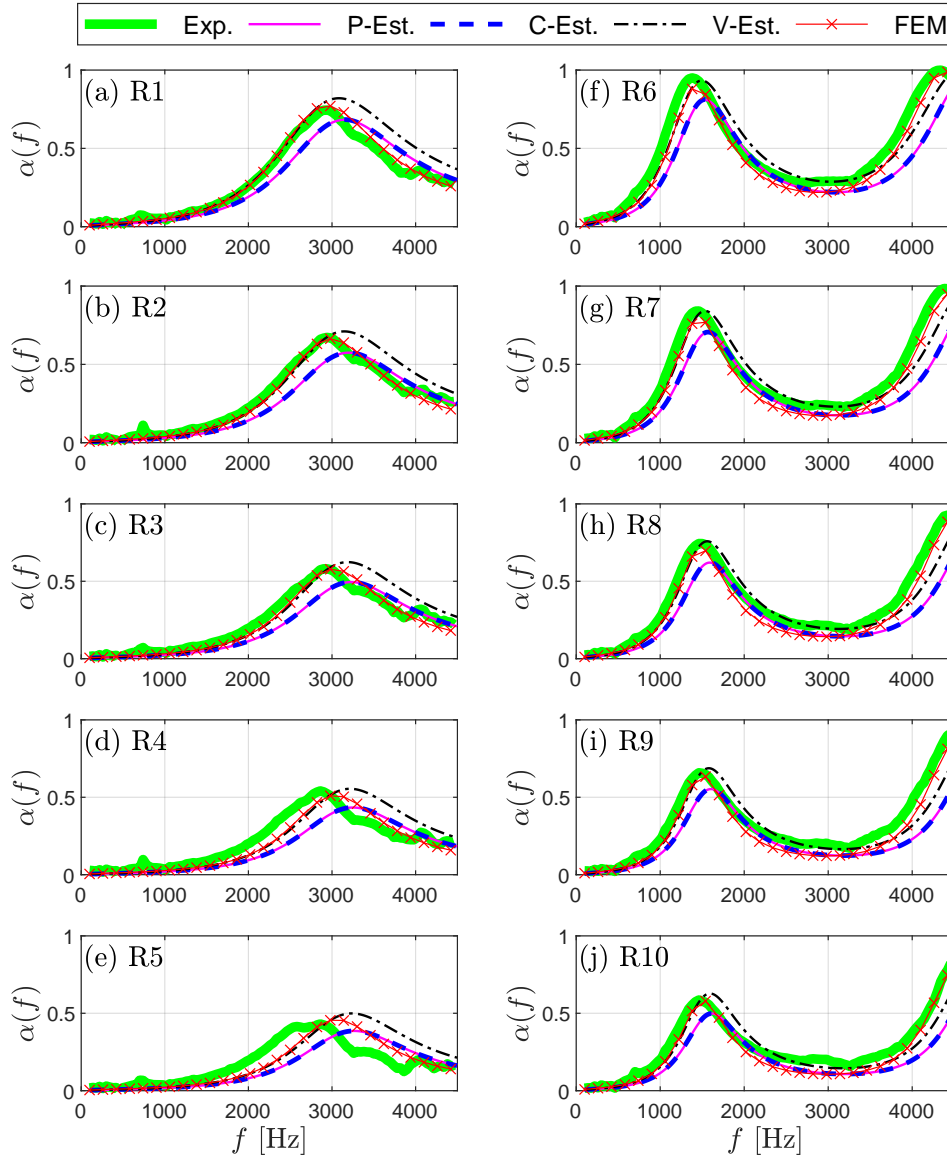


FIG. 19. Normal incidence SAC of samples R1 to R5 (left panels a-e) and R6 to R10 (right panels f-j): experiments (green thick continuous line), predictions [P-estimate (magenta continuous line), C-estimate (blue dashed line), and V-estimate (black continuous line)], and FE computations (line with cross markers).

- 525 <sup>3</sup>M. A. Biot, “Theory of propagation of elastic waves in a fluid-saturated porous solid. II.  
526 higher frequency range,” *J. Acoust. Soc. Am.* **28**(2), 179–191 (1956).
- 527 <sup>4</sup>K. Attenborough, “Acoustical characteristics of porous materials,” *Phys. Rep.* **82**(3), 179–  
528 227 (1982).
- 529 <sup>5</sup>D. L. Johnson, J. Koplik, and R. Dashen, “Theory of dynamic permeability and tortuosity  
530 in fluid-saturated porous media,” *J. Fluid Mech.* **176**(1), 379–402 (1987).
- 531 <sup>6</sup>Y. Champoux and J. F. Allard, “Dynamic tortuosity and bulk modulus in air-saturated  
532 porous media,” *J. Appl. Phys.* **70**(4), 1975–1979 (1991).
- 533 <sup>7</sup>D. Lafarge, “Propagation du son dans les matériaux poreux à structure rigide saturés  
534 par un fluide viscothermique: Définition de paramètres géométriques, analogie electro-  
535 magnétique, temps de relaxation (English translation: Sound propagation in rigid porous  
536 materials saturated with a viscothermal fluid: Geometrical parameters, electromagnetic  
537 analogy, relaxation times and universality theory),” Ph.D. thesis, Le Mans, France, 1993.
- 538 <sup>8</sup>S. R. Pride, F. D. Morgan, and A. F. Gangi, “Drag forces of porous-medium acoustics,”  
539 *Phys. Rev. B* **47**(9), 4964 (1993).
- 540 <sup>9</sup>D. Lafarge, P. Lemarinier, J. F. Allard, and V. Tarnow, “Dynamic compressibility of air in  
541 porous structures at audible frequencies,” *J. Acoust. Soc. Am.* **102**(4), 1995–2006 (1997).
- 542 <sup>10</sup>K. V. Horoshenkov, A. Hurrell, and J.-P. Groby, “A three-parameter analytical model  
543 for the acoustical properties of porous media,” *The Journal of the Acoustical Society of*  
544 *America* **145**(4), 2512–2517 (2019).

545 <sup>11</sup>B. Semeniuk and P. Göransson, “Microstructure based estimation of the dynamic drag  
546 impedance of lightweight fibrous materials,” *The Journal of the Acoustical Society of*  
547 *America* **141**(3), 1360–1370 (2017).

548 <sup>12</sup>B. Semeniuk, P. Göransson, and O. Dazel, “Dynamic equations of a transversely isotropic,  
549 highly porous, fibrous material including oscillatory heat transfer effects,” *The Journal of*  
550 *the Acoustical Society of America* **146**(4), 2540–2551 (2019).

551 <sup>13</sup>B. Semeniuk, E. Lundberg, and P. Göransson, “Acoustics modelling of open-cell foam  
552 materials from microstructure and constitutive properties,” *The Journal of the Acoustical*  
553 *Society of America* **149**(3), 2016–2026 (2021).

554 <sup>14</sup>J. L. Auriault and E. Sánchez-Palencia, “Etude du comportement macroscopique d’un  
555 milieu poreux saturé déformable (English translation: Study of the macroscopic behavior  
556 of a deformable saturated porous medium),” *J. de Mécanique* **16**(4), 575–603 (1977).

557 <sup>15</sup>E. Sánchez-Palencia, “Non-homogeneous media and vibration theory,” *Lect. Notes Phys.*  
558 **127** (1980).

559 <sup>16</sup>J. L. Auriault, “Dynamic behaviour of a porous medium saturated by a newtonian fluid,”  
560 *Int. J. Eng. Sci.* **18**(6), 775–785 (1980).

561 <sup>17</sup>S. Gasser, F. Paun, and Y. Bréchet, “Absorptive properties of rigid porous media: Ap-  
562 plication to face centered cubic sphere packing,” *J. Acoust. Soc. Am.* **117**(4), 2090–2099  
563 (2005).

564 <sup>18</sup>J. Allard and N. Atalla, *Propagation of sound in porous media: Modelling sound absorbing*  
565 *materials 2e* (John Wiley & Sons, 2009).

- 566 <sup>19</sup>T. G. Zieliński, R. Venegas, C. Perrot, M. Červenka, F. Chevillotte, and K. Attenborough,  
567 “Benchmarks for microstructure-based modelling of sound absorbing rigid-frame porous  
568 media,” *J. Sound Vib.* **483**, 115441 (2020).
- 569 <sup>20</sup>M. Yang and P. Sheng, “Sound absorption structures: From porous media to acoustic  
570 metamaterials,” *Annu. Rev. Mater. Res.* **47**, 83–114 (2017).
- 571 <sup>21</sup>Z. Laly, R. Panneton, and N. Atalla, “Characterization and development of periodic acous-  
572 tic metamaterials using a transfer matrix approach,” *Appl. Acoust.* **185**, 108381 (2022).
- 573 <sup>22</sup>J. Cuenca, P. Göransson, L. De Ryck, and T. Lähivaara, “Deterministic and statistical  
574 methods for the characterisation of poroelastic media from multi-observation sound ab-  
575 sorption measurements,” *Mech. Syst. Signal Process.* **163**, 108186 (2022).
- 576 <sup>23</sup>M. J. Bianco, P. Gerstoft, J. Traer, E. Ozanich, M. A. Roch, S. Gannot, and C.-A.  
577 Deledalle, “Machine learning in acoustics: Theory and applications,” *J. Acoust. Soc. Am.*  
578 **146**(5), 3590–3628 (2019).
- 579 <sup>24</sup>J. H. Jeon, E. Chemali, S. S. Yang, and Y. J. Kang, “Convolutional neural networks  
580 for estimating transport parameters of fibrous materials based on micro-computerized  
581 tomography images,” *J. Acoust. Soc. Am.* **149**(4), 2813–2828 (2021).
- 582 <sup>25</sup>M. Raissi, P. Perdikaris, and G. E. Karniadakis, “Physics-informed neural networks: A  
583 deep learning framework for solving forward and inverse problems involving nonlinear  
584 partial differential equations,” *J. Comput. Phys.* **378**, 686–707 (2019).
- 585 <sup>26</sup>S. De, J. Britton, M. Reynolds, R. Skinner, K. Jansen, and A. Doostan, “On transfer  
586 learning of neural networks using bi-fidelity data for uncertainty propagation,” *Int. J.*

587 Uncertain. Quantif. **10**(6) (2020).

588 <sup>27</sup>K. Bhattacharya, B. Hosseini, N. B. Kovachki, and A. M. Stuart, “Model reduction and  
589 neural networks for parametric pdes,” *SMAI J. Comput. Math.* **7**, 121–157 (2021).

590 <sup>28</sup>G. J. Lord, C. E. Powell, and T. Shardlow, *An Introduction to Computational Stochastic*  
591 *PDEs*, Cambridge Texts in Applied Mathematics (Cambridge University Press, 2014).

592 <sup>29</sup>I. Goodfellow, Y. Bengio, and A. Courville, *Deep learning* (MIT press, 2016).

593 <sup>30</sup>S. J. Pan and Q. Yang, “A survey on transfer learning,” *IEEE Trans. Knowl. Data Eng.*  
594 **22**(10), 1345–1359 (2009).

595 <sup>31</sup>K. Weiss, T. M. Khoshgoftaar, and D. Wang, “A survey of transfer learning,” *J. Big Data*  
596 **3**(1), 1–40 (2016).

597 <sup>32</sup>T. Iwase, Y. Izumi, and R. Kawabata, “A new measuring method for sound propagation  
598 constant by using sound tube without any air spaces back of a test material,” in *INTER-*  
599 *NOISE and NOISE-CON Congress and Conference Proceedings*, Institute of Noise Control  
600 Engineering (1998), Vol. 1998, pp. 1265–1268.

601 <sup>33</sup>O. Doutres, Y. Salissou, N. Atalla, and R. Panneton, “Evaluation of the acoustic and  
602 non-acoustic properties of sound absorbing materials using a three-microphone impedance  
603 tube,” *Appl. Acoust.* **71**(6), 506–509 (2010).

604 <sup>34</sup>V. V. Dung, R. Panneton, and R. Gagné, “Prediction of effective properties and sound  
605 absorption of random close packings of monodisperse spherical particles: Multiscale ap-  
606 proach,” *J. Acoust. Soc. Am.* **145**(6), 3606–3624 (2019).

- 607 <sup>35</sup>V. Voronina and K. Horoshenkov, “Acoustic properties of unconsolidated granular mixes,”  
608 Appl. Acoust. **65**(7), 673–691 (2004).
- 609 <sup>36</sup>H. K. Kim and H. K. Lee, “Acoustic absorption modeling of porous concrete considering  
610 the gradation and shape of aggregates and void ratio,” J. Sound Vib. **329**(7), 866–879  
611 (2010).
- 612 <sup>37</sup>W. S. Jodrey and E. M. Tory, “Computer simulation of isotropic, homogeneous, dense  
613 random packing of equal spheres,” Powder Technol. **30**(2), 111–118 (1981).
- 614 <sup>38</sup>W. S. Jodrey and E. M. Tory, “Computer simulation of close random packing of equal  
615 spheres,” Phys. Rev. A **32**(4), 2347 (1985).
- 616 <sup>39</sup>E. Ghossein and M. Lévesque, “A fully automated numerical tool for a comprehensive  
617 validation of homogenization models and its application to spherical particles reinforced  
618 composites,” Int. J. Solids Struct. **49**(11-12), 1387–1398 (2012).
- 619 <sup>40</sup>J. L. Auriault, C. Boutin, and C. Geindreau, *Homogenization of coupled phenomena in*  
620 *heterogenous media*, Vol. **149** (John Wiley & Sons, 2010).
- 621 <sup>41</sup>M. Avellaneda and S. Torquato, “Rigorous link between fluid permeability, electrical con-  
622 ductivity, and relaxation times for transport in porous media,” Phys. Fluids A-Fluid **3**(11),  
623 2529–2540 (1991).
- 624 <sup>42</sup>Y. Achdou and M. Avellaneda, “Influence of pore roughness and pore-size dispersion in  
625 estimating the permeability of a porous medium from electrical measurements,” Phys.  
626 Fluids A-Fluid **4**(12), 2651–2673 (1992).

- 627 <sup>43</sup>J. Rubinstein and S. Torquato, “Diffusion-controlled reactions: Mathematical formulation,  
628 variational principles, and rigorous bounds,” *J. Chem. Phys.* **88**(10), 6372–6380 (1988).
- 629 <sup>44</sup>C. Boutin and C. Geindreau, “Estimates and bounds of dynamic permeability of granular  
630 media,” *J. Acoust. Soc. Am.* **124**(6), 3576–3593 (2008).
- 631 <sup>45</sup>C. Boutin and C. Geindreau, “Periodic homogenization and consistent estimates of trans-  
632 port parameters through sphere and polyhedron packings in the whole porosity range,”  
633 *Phys. Rev. E* **82**(3), 036313 (2010).
- 634 <sup>46</sup>D. Lafarge, *The equivalent fluid model (Chapter 6, Part II) in Materials and Acoustics*  
635 *Handbook, edited by C. Potel and M. Bruneau* (Wiley, Chichester).
- 636 <sup>47</sup>G. Cybenko, “Approximation by superpositions of a sigmoidal function,” *Mathematics of*  
637 *Control, Signals and Systems* **2**(4), 303–314 (1989).
- 638 <sup>48</sup>K. Hornik, M. Stinchcombe, and H. White, “Multilayer feedforward networks are universal  
639 approximators,” *Neural Networks* **2**(5), 359–366 (1989).
- 640 <sup>49</sup>S. Gasser, “Etude des proprietes acoustiques et mecaniques d’un materiau metallique  
641 poreux modele a base de spheres creuses de nickel (English translation: Study of  
642 acoustical and mechanical properties of a model porous metallic material made of hol-  
643 low nickel spheres),” Ph.D. thesis, Institut National Polytechnique de Grenoble, 2003.  
644 <https://tel.archives-ouvertes.fr/tel-00004438>.
- 645 <sup>50</sup>C. Y. Lee, M. J. Leamy, and J. H. Nadler, “Acoustic absorption calculation in irreducible  
646 porous media: A unified computational approach,” *J. Acoust. Soc. Am.* **126**(4), 1862–1870  
647 (2009).

648 <sup>51</sup>T. G. Zieliński, “Microstructure-based calculations and experimental results for sound  
649 absorbing porous layers of randomly packed rigid spherical beads,” *J. Appl. Phys.* **116**(3),  
650 034905 (2014).

651 <sup>52</sup>R. Venegas, “Microstructure influence on acoustical properties of multiscale porous mate-  
652 rials,” Ph.D. thesis, University of Salford, UK, 2011.